Fedorov, Fedor S.; Solomatin, Maksim A.; Uhlemann, Margitta; Oswald, Steffen; Kolosov, Dmitry A.; Morozov, Anatolii; Varezhnikov, Alexey S.; Ivanov, Maksim A.; Grebenko, Artem K.; Sommer, Martin; Glukhova, Olga E.; Nasibulin, Albert G.; Sysoev, Victor V.

Quasi-2D Co3O4 nanoflakes as an efficient gas sensor

ARTICLE

Quasi-2D Co$_3$O$_4$ Nanoflakes as Efficient Gas Sensor *versus* Alcohol VOCs†

Fedor S. Fedorov,*[a]†† Maksim A. Solomatin,[b,c]†† Margitta Uhlemann,[d] Steffen Oswald,[d] Dmitry A. Kolosov,[e] Anatolii Morozov,[a] Alexey S. Varezhnikov,[b] Maksim A. Ivanov,[b] Artem K. Grebenko,[a,f] Martin Sommer,[g] Olga E. Glukhova,[e,h] Albert G. Nasibulin,[a,i] and Victor V. Sysoev[b]

We study quasi-two-dimensional crystals of Co$_3$O$_4$ grown by electrochemical synthesis on Pt electrodes in nanoflake morphology to serve as a gas sensor. When synthesizing in aqueous electrolytes under applied electrical bias the material follows a self-hierarchical architecture to primarily appear as hexagonal nanoflakes, α-Co(OH)$_2$. Following heating up to 300 ºC in the air, the as-synthesized material transforms to Co$_3$O$_4$ preserving the original hierarchical morphology. The Co$_3$O$_4$ nanoflakes have been found to have remarkable chemiresistive response when exposed to various kinds of alcohol vapors, at low *ppm* concentrations in mixture with air, over a wide range of temperatures, up to 300 ºC with a detection limit down to *ppb* range in the direct dependence on the alcohol molecule weight. We explain observed features of the gas response of Co$_3$O$_4$ nanoflakes by a shift of electron density under VOCs chemisorption verified by DFT calculations.

Introduction

The current trends for a smart livelihood that deals with Internet-of-Things enhance a need in research and development of gas sensors and gas-analytical units.[1] The requirements to sensors are ordinarily considered in terms of high sensitivity, high selectivity, high stability, and fast response/recovery[2] to be mainly defined by functional properties of gas-sensitive material which serves as a key primary transducer of a chemical sensor.[3] The recent progress in nanotechnology-driven development of low-dimensional oxide structures justifies its prospects for the development of gas sensors due to governing their receptor function forced by charge carries localization under surface processes like chemisorption. Indeed, these structures are characterized by a high surface-to-bulk ratio and at the same time could stay stable when one or two dimensions are in a micrometer range. In particular, (quasi-)2D materials are of high interest which typically include nanosheets, nanomembranes, nanoplates, nanowalls with a thickness from few to tens nanometers.[2]

However, the application of these materials to develop sensor units is rather limited[4] because the device production protocols frequently require routine nanolithography procedures which are quite challenging due to dimension differences of particles and lack facile, effective and reliable strategies for their integration.[5]

Oxide-based nanomaterials are one of the most promising materials when considering chemiresistive gas sensors.[6] Their morphology is mainly favored by synthesis method which determines a nucleation type and growth rate of crystal planes.[7–9] While historically *n*-type semiconducting oxides were primarily studied for R&D of sensors in an extensive degree,[9] currently there is a high interest in *p*-type semiconductors[10] like a cobalt oxide.[11,12] This oxide has an indirect band gap of 1.6-2.2 eV whose *p*-type conductivity matures from over-stochiometric content of oxygen.[11–13] In difference to electron-driven semiconductors, the chemisorption of oxygen favors a formation of hole-accumulation layers nearby the p-type oxide surface. The amount of adsorbed oxygen in these oxides is much larger when compared to *n*-type ones due to associated redox reactions at the surface.[12,14]

Since pioneer research of cobalt oxide chemiresistive properties by Stetter[15] in relation to CO detection, the most studies on cobalt oxide sensors have employed heterostructures[11] as, for instance, hollow nanocages functionalized by PdO,[16] nano-coaxial *p*-Co$_3$O$_4$/*n*-TiO$_2$,[17] or Pd-loaded hollow hierarchical nanostructures,[18] etc.[12,19] Recently reported protocols enable the application of pristine cobalt oxide in morphology to vary from quasi-0D to 3D films[11,20–26] where 2D structures in the form of macrosheets of atomic-comparable width are mostly interesting.[5] Such structures could be produced by various synthesis approaches, among which the wet-chemical synthesis characterized by simplicity and good control of material

[a.] *Skolkovo Institute of Science and Technology, Moscow 121205, Russia.*
E-mail: f.fedorov@skoltech.ru
[b.] *Yuri Gagarin State Technical University of Saratov, Saratov 410054, Russia.*
[c.] *Saratov Branch of Kotelnikov Institute of Radioengineering and Electronics of RAS, Saratov 410019, Russia.*
[d.] *IFW Dresden, Dresden D-01171, Germany.*
[e.] *Saratov State University, Saratov 410012, Russia.*
[f.] *Moscow Institute of Physics and Technology, Dolgoprudniy 141701, Russia.*
[g.] *Institute for Microstructure Technology, Karlsruhe Institute of Technology (KIT), Eggenstein-Leopoldshafen, Germany.*
[h.] *I.M. Sechenov First Moscow State Medical University, Moscow 119991, Russia.*
[i.] *Aalto University, Aalto 00076, Finland.*
†Electronic Supplementary Information (ESI) available: See DOI: 10.1039/x0xx00000x
††these authors contributed equally to this work.

dimensions to employ primarily hydro/solvothermal routes,[27] solvent evaporations, and other bottom-up strategies[2] like ones for fabrication of hollow microspheres.[28] There are already efforts to employ Co_3O_4 nanosheets synthesized by hydrothermal methods for NH_3 detection[29] or as sensors to acetone,[30] ethanol,[31] and humidity vapors.[32] However, the described methods still lack control over the amount of the material placed onto sensor contacts including the thickness of the layer and density of the particles. A direct bottom-up growth or direct positioning of the 2D material would advance the possibilities to locally design gas-analytical systems at single chips.

The most powerful technique to address a precise bottom-up growth of the oxide is realized via a known electrochemical approach which found primary a great interest in cobalt oxide synthesis for energy storage devices with advanced characteristics.[33] The synthesis includes mainly a generation of the base, i.e. production of OH^- species or a proton consumption nearby the electrode surface under application of electric fields in aqueous solutions of cobalt salts.[34] The obtained deposits appear directly on electrodes in the structure of oxide or hydroxide which could be further transformed to oxide. The process could be adjusted to synthesize the cobalt oxide in quasi-2D nanosheet morphology due to a base action that ordinarily impedes a growth of (111) facets that leads to exposing oxygen atoms/ions to the surface.[35,36] The process is easy to control by variation of deposition parameters like the electrode potential, steering, and electrolyte composition; the deposited mass is usually in a good agreement with consumed charge. The technique also enables rather fast producing the thin nanostructured layers at fine local morphology.[34,37,38] However, we still miss a systematic study on how to utilize such a deposition method to develop a good gas sensor with locally adjusted functional properties to be applied, for example, as alcohol vapor detectors which are important for healthcare applications.[39] Considering the advantages of the method, we believe that is the first study to employ it for the fabrication of gas sensors.

Here we explore gas-sensing properties of electrochemically-grown cobalt oxide quasi-2D nanoflakes towards various alcohol volatile organic compounds (VOCs) at low *ppm* concentration range in a mixture with air and explain their sensing properties via modeling the electron localization at the oxide surface subject to the vapor molecule adsorption by density functional theory (DFT). We demonstrate that the nanodimensionality of the grown oxide structures and their percolation-nature hierarchical arrangement enables effective transduction of surface chemisorption processes into a chemiresistive signal with detection limit *versus* alcohols going down to *sub-ppm* concentrations.

Experimental

Electrochemical deposition of the cobalt oxide layer

The electrochemical synthesis was performed in a potentiostatic mode using potentiostat-galvanostat Elins P-40X

(Elins, Russia). We utilized a three-electrode cell configuration with $Ag/AgCl_{sat.}$ electrode serving as the reference one which has a potential of 0.197 V *vs.* standard hydrogen electrode (ESI†, Figure S1). All the potentials were quoted in relation to this reference electrode. We employed a graphite rod as a counter electrode. Two types of working electrodes were utilized. To test the deposition conditions and mass of deposited material *versus* charge we used Au electrode with an area of 0.41 cm². For a sensor preparation, Pt multiple electrode stripes were used as a working electrode fabricated onto Si/SiO_2 substrate, 9x10 mm². These stripes were about 100 μm width, 4 mm length, which comprised a total metallization area of ca. 0.02 cm². The Si/SiO_2 substrate had also two Pt thermoresistors of ca. 1 μm thickness at the frontside, while the backside had four sputtered meander-shaped Pt heaters.[40,41] The thermoresistors and heaters were free to feed by electric potential during the electrochemical deposition. The electrochemical deposition was carried out in an electrolyte containing 0.1 M $Co(NO_3)_2$ at pH 5.4–6 under room temperature; the deposition potential was set to $E = -1$ V *vs.* $Ag/AgCl_{sat.}$ following results of previous studies.[36] Prior to the synthesis, we rinsed the electrode with a 10 % HCl aqueous solution, cleaned it with deionized water and then dried. All chemicals were of analytical purity. When synthesizing oxide nanostructures on the chip surface with multiple stripe electrodes, as a quantitative measure we utilized a deposition time derived in our experiments to correspond to the charge consumed under the potentiostatic mode.

Characterization of the cobalt oxide nanostructures by analytical techniques

In order to find out a correlation between the amount of deposited material and the charge utilized under the potentiostatic deposition, the mass of deposited material was estimated with inductively coupled plasma optical emission spectroscopy (ICP-OES). To perform it we synthesized a cobalt hydroxide on the Au electrode using the charge values from 0.1 C to 0.5 C with 0.1 C step. A starting point of 0.1 C has been chosen based on the analysis of recorded current transients. Following the deposition, the pristine cobalt hydroxide was dissolved in diluted H_2SO_4 acid. The cobalt content was analyzed by ICP-OES and further recalculated to a mass of $Co(OH)_2$ assuming that only this compound is deposited. To characterize the material under heating, including its application at the chip, we annealed the deposits in the oven (Nabertherm, Germany) at temperatures equal to 100 °C, 200 °C, and 300 °C under annealing times of 25 min, 50 min, and 250 min.

The morphology of the material was evaluated by scanning electron microscopy (SEM) using AURIGA® CrossBeam® workstation (Carl Zeiss, Germany) at an accelerating voltage of 5 kV. The oxidation of the deposited material and its stability at elevated temperatures was assessed by simultaneous thermal analysis (STA), a combination of differential temperature analysis (DTA) and thermogravimetric analysis (TGA) in the couple with mass-spectrometry (MS). Our tests included, 1) heating up to 550 °C which was much greater than the

operation temperature of the sensor, and 2) stability measurements where we observed the thermal behavior of the material under isothermal conditions for 4 h. We performed the measurements with NETZSCH STA 449 F3 Jupiter® unit combined with 403 Aëolos Quadro quadrupole mass spectrometer (NETZSCH-Gerätebau GmbH, Germany). For the measurements, the material was carefully collected from the electrode where it was deposited and then placed into alumina crucible. The experiment was done in a silicon carbide furnace; the device was vacuumized before each experiment. All the experiments were performed in the atmosphere of synthetic air. To examine a thermal behavior of the material in greater temperature range we used heating from 35 °C to 550 °C. Based on these results, we conducted the tests with heating in a range from 35 °C to 200 °C and from 35 °C to 300 °C followed by isothermal maintaining the material at the set temperature of 200 °C or 300 °C, respectively, for 4 h. The heating rate was set to 10 °C/min in all the experiments. During the measurements, we acquired the ion currents for the following mass-to-charge ratios (M/Z), M/Z=1, 2, 18, 40, 44.

To confirm a crystal phase of the materials, we transferred the material in as-deposited or annealed states onto double-sided adhesive tape. The X-ray diffraction (XRD) patterns were acquired using Bruker D8 advance diffractometer (Bruker, Germany) with Bragg-Brentano geometry and CuKα radiation source, λ=1.5418 Å. The XRD patterns were collected in the range of 2θ = 10-70° with a step of 0.0098° to be processed with @Eva4.3 software.

We studied the chemical composition of the material by X-ray photoelectron microscopy (XPS) with SPECS Phoibos 100 system (SPECS, Germany), 300 W, using MgKα-source, hν = 1253.6 eV, at pass energy equal to 15 eV. We referenced all the spectra to the C 1s peak of hydrocarbon, 285.0 eV binding energy, to be controlled through known peaks of metallic Cu, Ag, and Au. The C 1s, O1s, and Co2p core level spectra were acquired and refined by multiple scanning. We performed deconvolution of the obtained multicomponent spectra by means of @MultiPak software package (Physical Electronics, USA) employing Lorentz-Gauss functions for peaks approximation.

For the transmission electron microscopy (TEM) studies, we prepared a sample by loading the material of interest to isopropanol solution and depositing drops of the suspension onto a carbon film supported by a copper grid. Bright field (BF), dark field (DF) images, including dynamic dark field imaging with circle rotation of objective aperture, as well as selected area electron diffraction (SAED) patterns were acquired with FEI Tecnai G^2 F20 S transmission electron microscope (Eindhoven, The Netherlands) equipped with EDAX detector for energy dispersive x-ray analysis (EDX) at an acceleration voltage of 200 kV. The phase analysis and preferential growth direction identification were carried out using @SingleCrystal 2.3.3 software.

The multielectroded chip

In this study, we used a multielectroded chip as a platform for the synthesis of materials and further measurement of its

electrical properties when exposed to various environments. The chip represented the Si/SiO$_2$ substrate, 9x10 mm^2, with sputtered co-planar multiple-strip Pt electrodes, the thickness of ca. 1 μm, distanced at gaps of ca. 80 μm.[40] Every two Pt electrodes defined a single chemiresistive sensor. The chip was also equipped with two calibrated meander Pt thermoresistors at the frontside to control the operating temperature. The heating facility was ensured via four Pt meander heaters at the backside of the chip. The control over temperature was carried with an accuracy of ca. 0.1 °C by a proportional–integral–derivative controller under operation by the home-made electronic scheme. Still, the temperature uncertainty under the actual chip operation can be ±10 °C because of thermal Si/SiO$_2$ substrate properties.[41,42] At the temperature of 275 ºC the total power consumption which is managed by chip size and the geometry of the applied heaters was about 3 W.

In the paper, we deliver data for one chip which was consistently measured under all the reported conditions while a few more chips were partly employed in the course of the study at different stages.

Gas-sensing and electrical measurements

We tested the response of the Co$_3$O$_4$ nanoflakes-based sensors at the multielectrode chip to alcohol VOCs in the mixture with pure air. The setup consisted of a data acquisition unit, generator of analyte vapors and a unit to control the chip operation temperature, all managed by PC as shown in ESI† (Figure S2).

The home-made unit for data acquisition was based on National Instruments multi-port board USB-6259 being combined with low-noise current pre-amplifier (SR570, Stanford Research Systems) to enable one measuring a wide range of resistances, up to tens of GOhms. All the sensor elements in the chip were read out in sequence via multiplexing cards at the rate lower than 1 s per each element. The resistance was stored to PC by measuring a current through the sensor element under study while applying a constant d.c. voltage. The test vapors were generated by a gas generator (OVG-4, Owlstone, UK) based on permeation tubes.[43] We supplied a filtered lab air to be dried by the corresponding unit (PG14L, Peak Scientific, UK) as a background gas in the experiments. The analytes of alcohol VOCs, methanol, ethanol, isopropanol, and butanol, were added to the air in a flow-mode at concentrations of 1- 10 ppm range by forking the flows in the corresponding ratios. The gas flow rate was maintained with the help of precision mass-flow controllers (Bronkhorst, The Netherlands) at the level of 100 sccm. In order to test a humidity effect, the bubbler containing distilled water was supplied to the gas flow in a required ratio. For measurements, the chip with Co$_3$O$_4$ nanoflakes-based sensors was mounted into a sealed stainless-steel chamber where the chip frontside has been washed by the incoming gas flow.[44] We exposed the chip to the vapors by series for 2 h duration interrupted by exposure to pure air for more than 2 h. The operation temperature was adjusted in a range from room one to 300 °C and has been varied with a step of 25 °C.

The chemiresistive response is calculated as $S= \Delta R/R_{air}$, also in percent, where R_{air} and ΔR denote the resistance of the Co_3O_4 nanoflake layer in air and its change in the presence of alcohol VOCs when mixed with air, respectively.

To confirm the origin of charge carrier type in the Co_3O_4 nanoflake layer on the chip, field-effect transistor (FET) measurements were performed in top contact bottom gate geometry with ca. 80 μm wide and ca. 4 mm long channel formed by cobalt oxide layer employing four-probe station connected to the semiconductor analyzer Keysight B1500A (Keysight Technologies, US) as detailed in ESI† (Figure S3). The two sensor measuring electrodes served as a source and drain ones at constant V_{SD} bias while the gate potential was applied to the chip Si substrate and swept in [-40:+10] V range. SiO_2, ca. 300 nm thick, served as a bottom gate insulator.

Impedance spectroscopy

To measure the full impedance of Co_3O_4 nanoflakes-based sensors, Z, we employed impedance meter NovoControl Alpha AN (Novocontrol Technologies, Germany) capable to test the impedance-to-frequency function, $Z(f)$, in a wide range of frequencies, 10^{-2}-10^7 Hz. We have limited the frequency range by 1-10^7 Hz values because lower ones required an extensive reading-out time while delivering data close to d.c. measurements. We conducted two sets of experiments applying the a.c. voltage at amplitudes equal to 0.1 V and 5 V. The sensors at the chip were heated up to 300 °C, equal to the operating temperature, optimal for chemiresistive effect observation as revealed at gas response tests taken under d.c. measurements.

Computational details

We conducted *in silico* study of the interaction of alcohol molecules with Co_3O_4 crystal surface using the self-consistent charge-density functional tight binding (SCC DFTB) method[45] which is shown to be efficient for calculating energy and electronic structure of crystals whose supercells contain hundreds or even thousands of atoms.[46,47] For comparison, *ab initio* methods allow one studying structures with supercells containing no more than 100-150 atoms which is drastically limited by the employed basis set of atomic orbitals, especially at s-, p-, and d- ones. At the same time, the SCC DFTB method gives opportunities to extend the number of atoms in supercell up to 200-500 ones. This method was realized here in frames of @DFTB+[48], @Kvazar and @Mizar[49] software packages.

In order to assess the Co_3O_4 surface conductivity in dependence on adsorbed molecules, and its relative change, $\Delta R/R_0$, as chemiresistive response, we have utilized self-consistent charge-density functional tight binding, SCC DFTB, method under the Keldysh nonequilibrium Green Function technique and Landauer–Büttiker formalism,[45] realized in the mentioned software packages.

Results and discussion

Electrochemical synthesis of the functional layer

First, we have evaluated the features of the material to be deposited as a hydroxide on Au electrodes. The electrochemical deposition conducted in a potentiostatic mode at -1 V *vs.* Ag/AgCl$_{sat.}$ demonstrates a monotonous decay of current with time (Figure 1a). This process results in sedimentation of $Co(OH)_2$ due to a base appearance following reduction of nitrate ions as described by [50–53]

$$NO_3^- + H_2O + 2e^- \rightarrow NO_2^- + 2OH^- \qquad (1)$$

$$Co^{2+} + 2OH^- \rightarrow Co(OH)_2 \qquad (2)$$
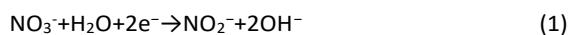
The current transient $j(t)$ goes to be linear if to plot the dependence at Cottrell coordinates what normally hints on the diffusion-limited process (Figure 1a, inset).[54,55] We have calculated the diffusion coefficient according to the Cottrell equation to be ca. $3.52·10^{-6}$ cm^2s^{-1} which could be considered as an effective, $D_{eff.}$, value because the whole deposition might further include various possible nitrate reaction pathways[52,53,56,57] and chemical reaction of sedimentation, eq. (2).

Further, we have assessed a consumed charge related to the surface area, i.e. specific charge, as a quantitative indicator of deposited mass. Figure 1b shows the charge dependence on the deposition time displaying a monotonic reduction of the charge. When the specific charge reaches the value of ca. 0.5 C/cm^2 the transient goes almost linear with the time that supports mass-controlled kinetics of the deposition process. As one can see in Figure 1b, the mass of deposited material estimated by ICP-OES depends on the charge almost linearly in -0.5 … -1.25 C/cm^2 range. Notably, the measured mass slightly exceeds one calculated by Faraday law according to equations (1) and (2) when considering 100 % efficiency of material transformation.[58] This might be due to a contribution of other electrochemical processes anticipated to occur at this potential.[51] At the same time, the current transient $j(t)$ recorded in a supporting electrolyte of 0.2 M $NaNO_3$ shows a similar behavior *on par* with cyclic voltammetry results which suggest the cathodic processes to occur at about -0.25 V and -1 V favoring a generation of a base (see ESI†, Figure S4). Thus, these results hint that deposition is mass-controlled at longer times; the deposited mass correlates well to the consumed charge what enables rather simple control of the amount of deposited material. Further, we have utilized the deposition time as a major parameter to control the consumed specific charge.

When deposited on the Au electrode the material represents a rather dense though porous film comprised of interconnected flakes (Figure 1c) architecture which is favorable for gas sensor development due to high surface-to-volume ratio. Therefore, we have applied the same approach to the deposition of cobalt oxide on Si substrate equipped with multiple Pt strips[59] to develop gas-sensitive layers. In preliminary studies, we have not found large differences in the morphology of cobalt oxide when employing the same protocols for deposition at Pt electrodes. Indeed, the material crystallizes in a similar distinct morphology of nanoflakes whose lateral dimensions approach 0.2–0.5 μm while the thickness is still in the range of nanometers or tens of nanometers. Primarily, the material is grown at metal
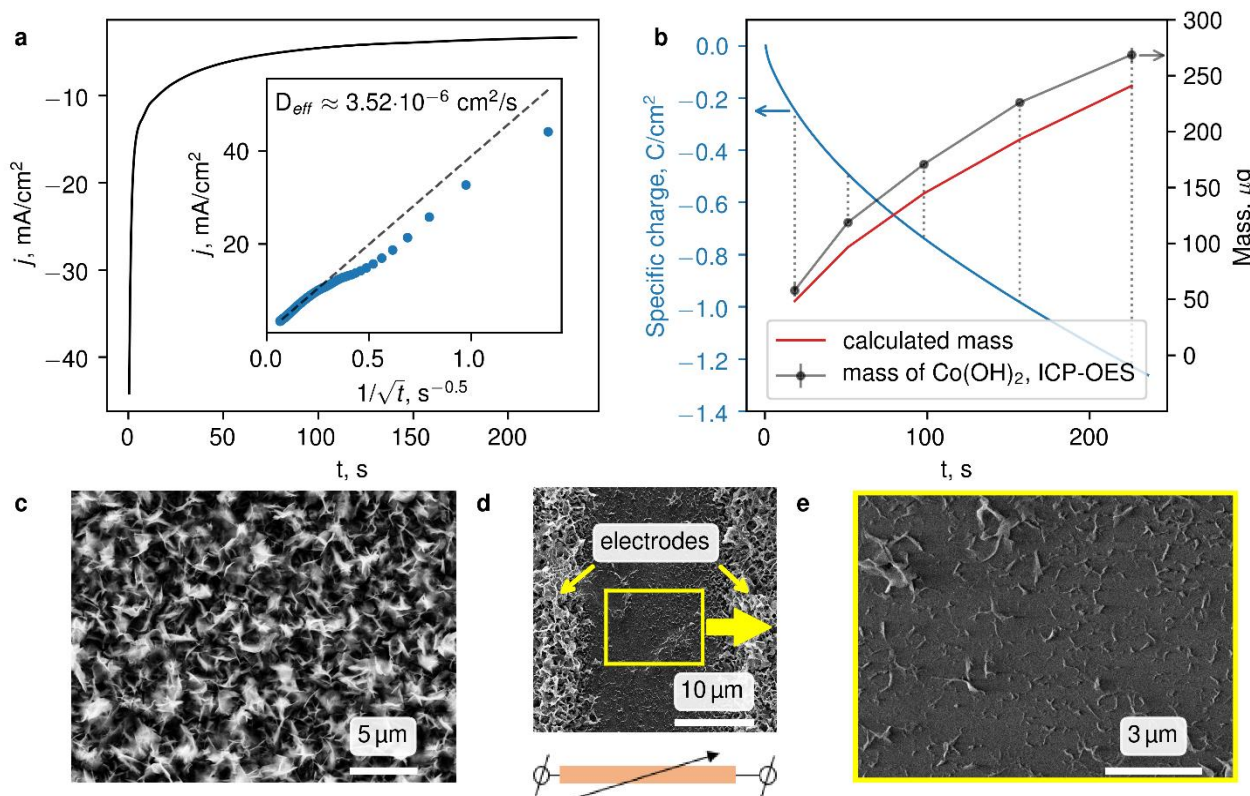
Figure 1. Electrochemical deposition of cobalt hydroxide: a) current density transient for deposition of cobalt hydroxide on flat Au electrode from 0.1 M Co(NO₃)₂ electrolyte at - 1.0 V vs Ag/AgClₛₐₜ reference electrode; insert: corresponding Cottrell plot; b) the consumed specific charge, corresponding measured and calculated mass *versus* a deposition time; c) morphology of the cobalt hydroxide deposited on flat Au electrode; d), e) overview of the morphology of cobalt oxide layer deposited on Pt electrodes of the chip at the macroscale (d) and microscale (e) in between-in electrode space; the time of deposition is equal to 75 s what corresponds to the specific charge of ca. 0.7 C/cm².

electrodes which are biased, but the material also extends out to the adjacent inter-electrode space on the dielectric, Si:SiO₂ substrate (Figure 1d,e). The hydroxide layer appeared at the dielectric is much thinner when compared to the one at the electrodes though it still bears the similar morphology of nanoflakes, more distant from each other compared to the electrode surface. The important feature is that the flakes form a matrix which provides conductance pathways between strip electrodes (Figure 1d).

Material characterization

Prior to the investigation of gas sensing properties, we have assessed thermal stability and chemical transformations of the deposited material induced by heating in air. Firstly, by heating up to 550 °C we have tried to survey the major phase transformations (Figure 2a) while secondly, we have focused on heating up to temperature range of 200 - 300 °C to match the sensor operation as further clarified (Figure 2b,c).

The heating of as-deposited material in air results in a primary mass change of ca. 3 % to occur at 80 °C that seems to be attributed to the removal of physisorbed water. It is followed by a mass loss step at about 165 °C what is characterized by increasing the yield at about 195 °C manifested as a steeper slope of the TG curve with further mass reduction till 210 °C under lower steepness. At the temperature of about 400 °C we

observe a mass stabilization. The ion current of water clearly corresponds to these changes demonstrating the onset of liberation peak at about 150 °C and the second peak at about 190 °C with restoration to background values at about 280 °C. The DTA curve follows these changes exhibiting broad and steeper endothermal peaks close to the temperatures related to the observed changes. The residual mass is about 79 % at 550 °C while at the temperatures of 200 °C and 300 °C the residual mass comprises 85 % and 81 %, correspondingly. The overall process might be schematically described as[60]

$$3Co(OH)_2 \cdot 2H_2O + 1/2O_2 = Co_3O_4 + 5H_2O \qquad (3)$$
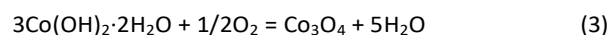
The total process according to eq. 3 should be characterized by a mass loss of ca. 18 % that agrees with the experimental values when excluding a loss due to physisorbed water.

When testing the thermal stability of the obtained material at 200 °C and 300 °C for 4 hours (Figure 2b,c) we observe in both cases a stabilization of mass after reaching the set temperature at the level of 82-84 %. Following the stabilization of mass, there is some reduction of ion current related to water. The increasing temperature results in a lower rate of water liberation because the slope of ion current is steeper in case of annealing
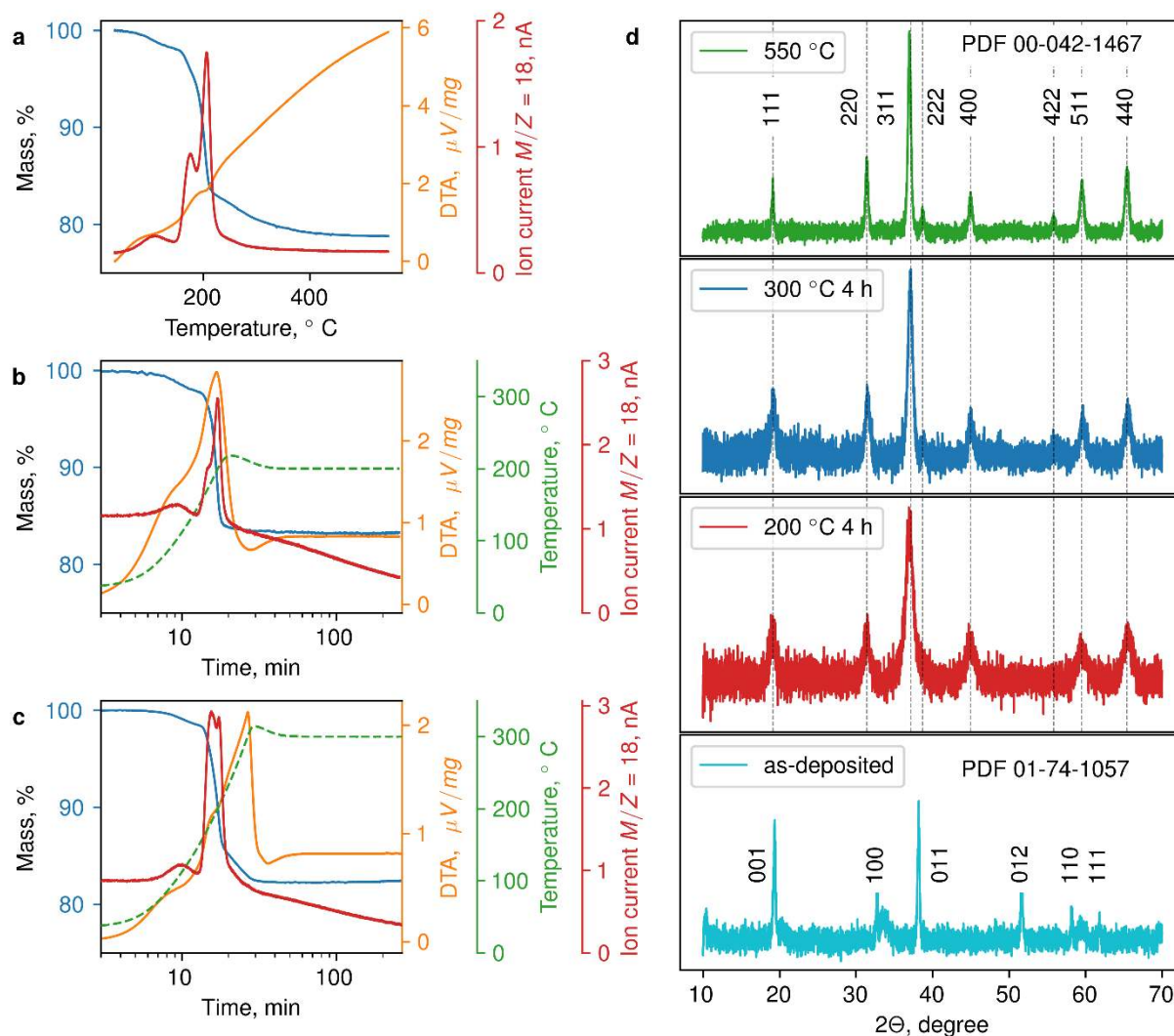
Figure 2. Characterization of thermal behavior of deposited cobalt hydroxide: a), b), c) STA-MS results of the deposited material when heated up to 550 °C, 200 °C and to 300 °C, respectively, in synthetic air with isothermal, 4 h, measurement performed for (b) and (c); (d) XRD results of the as-deposited material and the one after STA-MS studies at corresponding labeled temperatures.

temperature 200 °C when compared to one at 300 °C what suggests a greater degree of desorbed water.

The XRD patterns for as-deposited cobalt hydroxide and the one after annealing in synthetic air at 200 °C, 300 °C for 4 h and 550 °C just in the STA device are shown in the Figure 2d. As revealed by XRD, the deposited material crystallizes into α-$Co(OH)_2$ hexagonal phase, space group $P\overline{3}m1$ (PDF 01-74-1057) which is characterized by intensive 001, 011 and 012 peaks

observed at 19.35 °, 38.19 °, and 51.64 ° correspondingly, due to the appeared sheet-like morphology. These features hint at the appearance of some material texturing at the basal plane. Annealing at 200 °C, 300 °C, and 550 °C transforms the hydroxide into polycrystalline spinel-type Co_3O_4 oxide, a cubic phase, space group $Fd\overline{3}m$ (PDF 00-042-1467) with (111), (220), (311), (400), (511) and (440) planes.

Table 1 Assessment of full width at half maximum for cobalt oxide annealed at various temperatures.

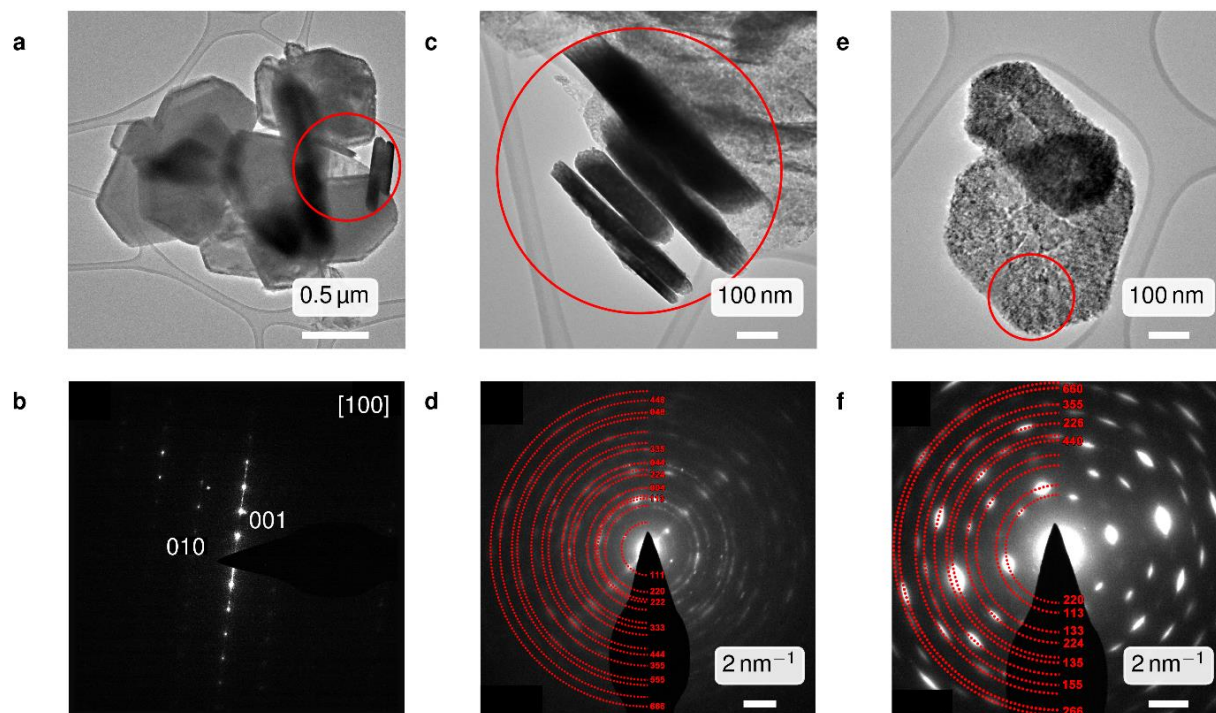| Co_3O_4 annealing conditions	FWHM, deg					
	111	220	311	400	511	440
200 °C (4 h)	1.52±0.06	1.35±0.06	1.43±0.02	2.02±0.09	2.20±0.103	1.69±0.06
300 °C (4 h)	0.88±0.03	0.71±0.02	0.793±0.07	0.78±0.04	0.88±0.04	0.88±0.03
550 °C	0.62±0.02	0.48±0.01	0.52±0.004	0.64±0.03	0.72±0.02	0.61±0.01

Figure 3. TEM characterization of cobalt oxide structures prepared by electrochemical deposition: a) bright field image (a) and SAED pattern (b) of the as-deposited sample; bright field images (c,e) and SAED pattern (d,f) of the samples annealed at 300 °C in the air for 4 h. The SAED patterns were collected from regions outlined with a red circle in (a,c,e).

We observe a gradual increase of the relative height of reflexes corresponding to better alignment of atoms in nanosheets, i.e. growth of the crystal size as annealing temperature enhances.

A usual routine involving the Debye-Scherrer equation is hardly applicable for crystals with such a pronounced anisotropy.[61,62] Therefore, we have assessed peak broadening fitted by Gaussian function corresponding to different planes of the XRD pattern of Co_3O_4 annealed at different temperatures. The results are assembled in Table 1.[63] The full width at half maximum indicates a decrease of broadening in about 3 times with the rise of the annealing temperature what is especially pronounced for (311) plane in accordance with enhancing a crystal size.

While the material deposited on electrode comprises agglomerated nanoflakes, we have further utilized TEM to observe the structure of single flakes that were drop-casted from isopropanol suspension of material picked from the electrode just after the deposition and following the annealing at 300 °C. The TEM images show the as-deposited material to be crystallized in the form of hexagonal plates with a width up to 1 micron and a thickness of 50-150 nm (Figure 3a, see also ESI†, Figure S5a,b) at α-Co(OH)$_2$ crystal structure (space group P$\bar{3}$m1, a ≈ 3.17 Å, c ≈ 4.64 Å), in a full coincidence with XRD patterns (Figure 3b). After annealing at 300 °C, the size and shape of the particles do not change (Figure 3e), however, the hexagonal structure of α-Co(OH)$_2$ is transformed into the cubic structure of spinel Co_3O_4, space group Fd$\bar{3}$m, a ≈ 8.08 Å. The bright field image, drawn in Figure 3e, indicates that the Co_3O_4 plates consist of a number of nanocrystals ranging in size from a few nanometers to tens of nanometers (also, see ESI†, Figure S5c,d). At the same time, selected area electron diffraction (SAED) patterns from this region do not exhibit rings as in the case of polycrystalline materials. Such a diffraction pattern is more typical for twinning or the location of several different single crystals in the region of the selector aperture.[64,65] It seems the crystals composing Co_3O_4 plates have a tendency to a mutual orientation that results in a formation of a pseudo-single-crystal structure at the quasi-2D shape. The [111] direction is normal to the "large" particle surface.

We have confirmed the chemical composition of the cobalt oxide surface by X-ray photoelectron spectroscopy (XPS). The core level spectra of Co 2p and O 1s acquired from the as-deposited material and from annealed one at 300 °C for 4 h are given in Figure 4a-e. Co 2p spectra are characterized by two spin-orbit doublets and two shake-up satellites. For as-deposited sample, we have observed Co 2p3/2 and Co 2p1/2 peaks which are distinguished to be separated by 15.8 eV with intense satellite structure what corroborates well with literature data for Co(OH)$_2$.[66,67] The peaks are observed at 780.8 eV and 796.6 eV, respectively. The energy distance between the first deconvoluted peak in Co 2p3/2 region denoted as peak A in Figure 4 and the first satellite is 5.4 eV while the second satellite is shifted at about 22.05 eV. The difference between the first deconvoluted peak in the region Co 2p1/2, peak A* in Figure 4, and the second satellite is 6.55 eV.

The annealed samples of Co_3O_4 are characterized by a weak satellite structure.[67] The Co 2p3/2 and Co 2p1/2 peaks are observed at 780.2 eV and 795.6 eV binding energies
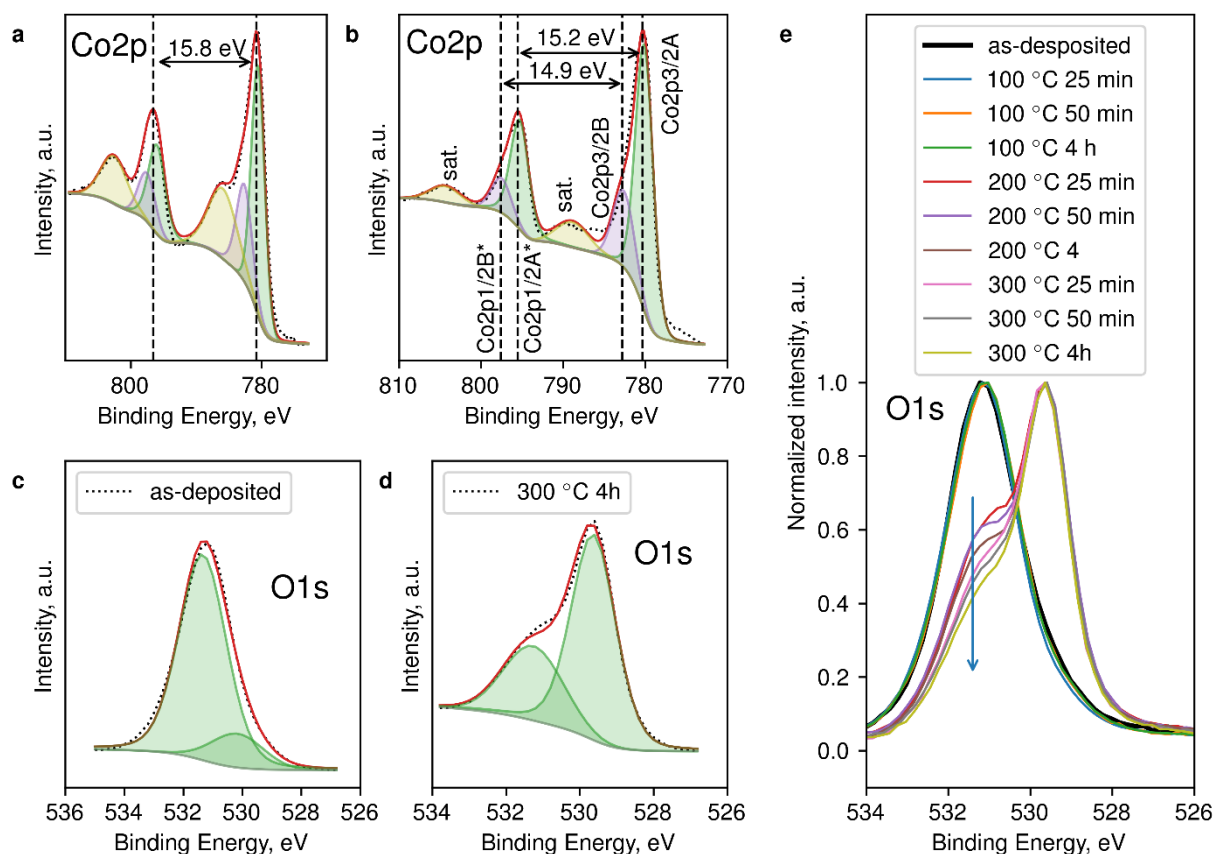
Figure 4. XPS characterization of cobalt oxide structures prepared by electrochemical deposition: a), b) cobalt core level spectrum forthe as-deposited material (a), and the one annealed at 300 °C for 4 h (b); c), d) oxygen core level spectrum for the as-deposited material (c) and the one annealed at 300 C for 4 h (d); e) oxygen spectra for the as-deposited material and the one annealed at 100 °C, 200 °C and 300 °C correspondingly for 25, 50 min and 4 h.

correspondingly what shows a chemical shift of 0.6 eV. Deconvoluted spectra enable us to distinguish six bands that are related to paramagnetic Co^{2+} in tetrahedral sites, diamagnetic Co^{3+} in octahedral sites and shake-up excitations.[68] The distance between the first satellite and peak A is estimated to be about 8.75 eV and the assessed difference in the position of peak A and the second satellite peak equals 24.25 eV. The peak A* is separated from satellite by 9.05 eV to be in good agreement with the literature.[68,69] The deconvoluted values are fully tabulated in ESI† (Tables S1-S2). In Figure 4c,d, the red line envelops a composite O 1s core level spectrum for as-deposited material and the one annealed at 300 °C for 4 hours which we have deconvoluted into two bands. In the case of as-deposited material we observe the most intensive low-energy band at 529.9 eV and a small peak at higher binding energy (531.3 eV) what correlates well with OH bonds and confirms the $Co(OH)_2$ structure. In the annealed samples the band related to lower binding energy is mainly pronounced at 529.6 eV to relate to Co-O bond while the second band is expressed in a shoulder positioned at 531.3 eV that hints on the appearance of OH surface species and/or adsorbed water (ESI†, Tables S3-S4). Thus, the differences in satellite structure of Co 2p and also the difference in O 1s line energies allow one to identify two phases, $Co(OH)_2$ and Co_3O_4 in accordance with literature.[70] $Co(OH)_2$ phase is stable even at elevated temperatures up to 100 °C. The overall composition ratio is derived based on spectra for both

as-deposited samples and Co_3O_4 ones, though, the calculation results overestimate O concentration (see ESI†, Table S5), probably due to a carbon influence. When taking into consideration samples annealed at 200 °C and 300 °C we could observe (Figure 4e) that the intensity of OH-related shoulder at O 1s spectra is reduced with temperature and with increase of annealing time. The related peak amplitude is reduced due to a desorption of OH species what corroborates well with STA-MS data which deal with water ion current (Figure 2b,c). We can assume that the desorption of OH/water moieties at elevated temperatures favors an appearance of O-ion species at the Co_3O_4 surface. This is accompanied by a decrease in surface carbon concentration. The similar trend has been also indicated elsewhere.[71]

Gas-Sensing properties

To study the chemiresistive properties, the cobalt oxide nanoflakes have been synthesized by electrochemical deposition over the multielectroded chip under the same protocol detailed in Experimental. We have varied the deposition time in the range from 25 s to 175 s. With a total of 39 electrodes located at the chip, we have biased every six electrodes to synthesize various amounts of the material at the same chip according to each deposition time. Prior measurements we have stabilized the chip, which carries a

number of sensors, at 300 °C for 24 h in air. The chemiresistive response of the sensors located at the chip, $S=(R_{gas}-R_{air})/R_{air}$, has been measured towards alcohol VOCs, methanol, ethanol, isopropanol, and butanol, at different operating temperatures. The employed chip platform is quite convenient for an evaluation of sensing properties of materials with induced variation, such as a mass of deposited material enabling high-throughput testing. The response of the sensors prepared under various synthesis time under operating temperatures within 175-300 °C range is given in the Figure 5a *versus* four alcohol VOCs; all the analytes are mixed with pure air, 10 ppm concentration. Below 175 °C we have not observed a response exceeding a noise. The response increases to a maximum at ca. 250-275 °C for all the Co_3O_4-based sensors followed by a decrease at more elevated temperatures. The maximum response is observed for the oxide films deposited using 75 s at 275 °C. It is shifted with temperature for sensors characterized by the deposition time lower than 75 s, where the oxide films appear in the finely dispersed structure which is more sensitive to inter-flake barriers when compared to more homogeneous films prepared under greater deposition time. Thus, enhancing the operation temperature in this semiconducting oxide results in a higher concentration of charge carriers and in facilitating the catalytic properties, as well as modulates the potential barriers enabling greater chemiresistive response.[42,72] Moreover, we observe a clearly pronounced dependence of the response with a molar mass of analyte in the studied homologous VOC series.

To study the existence of potential barriers, we have acquired I- V curves prior to each measurement of the sensors in air and vapors. Figure 5b shows exemplary I-V curves recorded in the air for one of the sensors under various operating temperatures, 175-300 °C range. The almost linear curves support the existence of Ohmic contacts, i.e. absence of Schottky barriers at the Co_3O_4-Pt interface. Still, the existence of the hole accumulation layer at the surface of the quasi-2D flakes of cobalt oxide affects the layer conductivity by localization of free charge carriers. Thus, the conduction mechanism is contributed by both a surface conductivity ("bulk") and modulation of the barriers ("boundary"). As the Debye length becomes comparable with the thickness of the oxide nanosheets the influence of barriers might be rather pronounced. To further evaluate the mechanism of conductivity, we have performed impedance spectroscopy applying different a.c. amplitude of bias, 0.1 V and 5 V.[73] The results are presented in Figure 5c as a dependence of imaginary part of impedance (Z_{im}) on its real part (Z_{real}), or Nyquist plot, for the exemplary sensor exposed to pure air.

The $Z(f)$ spectrum recorded in the air at 0.1 V of a.c. amplitude is represented by at least two semicircles allowing us to use an equivalent circuit consisting of two RC components responsible for the influence of "bulk" and "boundary" parts[74] (Figure 6c). A similar circuit has been already employed earlier (refs. [75,76]) and can be attributed to the "brick layer model"[77–79] which describes grain conductivity and grain boundaries conductivity in polycrystalline samples. The components constituents are denoted as R1, C1, R2 and CPE where R1 and C1 represent

"bulk" electrical properties while R2 and CPE belong to "boundary" ones. The constant phase element (CPE) is used in this case to describe capacitive properties of the system at lower frequencies (ref. [75]) usually attributed to charged species (ions and defects) and polarization effects (1):

$$CPE = 1/(T \times (iw)^p), \qquad (4)$$

where i is the imaginary unit, w is the angular frequency, T and p are the constants.

Thus, CPE should be fitted by two variables, T (CPE-T) and p (or CPE-P), to resemble a capacitor when CPE-P tends to 1. According to the mentioned model, the bulk properties of the layer under study are usually manifested at higher frequencies while grain properties should contribute to $Z(f)$ mainly at lower frequencies.[80] The spectrum of quasi-2D Co_3O_4 nanoflake layer measured in air at 0.1 V amplitude is indeed represented by two semicircles, one of which at low frequency domain gets depressed by applying the a.c. voltage at 5 V amplitude; the change is at ca. 10-30 kHz. It seems the higher a.c. voltage lets the free carriers to overcome the existing inter-flake potential barriers. We have fitted the obtained $Z(f)$ data using the described equivalent circuits to assess the values of circuit components. The fitted values are tabulated in ESI† (Table S6, data for other sensors fabricated using deposition time of 75 s are presented in Figure S6). As has been previously discussed, the "bulk" resistance and capacitance (R1, C1) are almost unchanged by the application of greater a.c. bias, while "boundary" components (R2 and CPE-T) are significantly modulated. It is worth noting that CPE-P is close to a unity hinting on a capacitive behavior. At frequencies lower than 70 Hz, one more RC component starts being pronounced what can be attributed to the effect of electrode.[74] Thus, we see that the electrical transport throughout the layer of quasi-2D Co_3O_4 nanoflakes is greatly influenced by barriers that could be responsible for the layer gas sensitivity, and hint on the formation of the percolative layer.[81] The changes brought by barriers are well pronounced at frequencies starting from 10 kHz with saturation at ca. 1 kHz as follows from $|Z|_{0.1V}/|Z|_{5V}$ (Figure 6c).

The exposure of the chip to alcohol VOCs in the mixture with air results in a reversible change in d.c. resistance under the ordinary operation of chemiresistors as shown in Figure 5d. The resistance goes up by few times of magnitude under the alcohol appearance whose change depends on the analyte concentration and its kind in accordance with the p-type conductivity of this material which is confirmed by transconductance FET measurements presented in ESI† (Figure S3). Formation of hole-accumulation layers characteristic for such p-type metal oxide gas sensors facilitates conductivity along the surface of such layer, which should favor the response when decreasing the characteristic size of the flakes and, importantly, by an improvement of inter-flake connection configuration.[12]

We have plotted the response-to-concentration dependence for all the alcohols under study in Figure 5e. As noted above, the enhancing molecular weight of analytes facilitates increasing in the chemiresistive response at the same analyte concentration. For instance, we observe approx. 420 %, 280 %, 220 %, and 140 % of resistance variation upon exposure to 10 ppm of butanol, isopropanol, ethanol, and methanol, correspondingly. These data are comparable with the highest values reported in the literature for various cobalt oxide nanostructures; see ESI†, Figure S10, Table S7. The sensors are characterized by non-linear concentration dependence which can be described by Freundlich isotherm (Figure 5e) with power degree index equal

to ca. 0.55 (methanol), 0.38 (ethanol), 0.22 (isopropanol) and 0.34 (butanol). The detection limit of these sensors goes down to *ppb* range of concentrations to be estimated as 92.2 ppb, 2.8 ppb, 0.004 ppb, and 0.15 ppb, correspondingly, for methanol, ethanol, isopropanol, and butanol under extension of Freundlich isotherm to this range (see ESI†, Figure S7);[82] still, these data might be refined when considering Wolkenstein isotherm.[83] The observed high vapor sensitivity clearly matures from the fine structures of the cobalt oxide appeared at the inter-electrode gap in the nanodimensional scale as given in
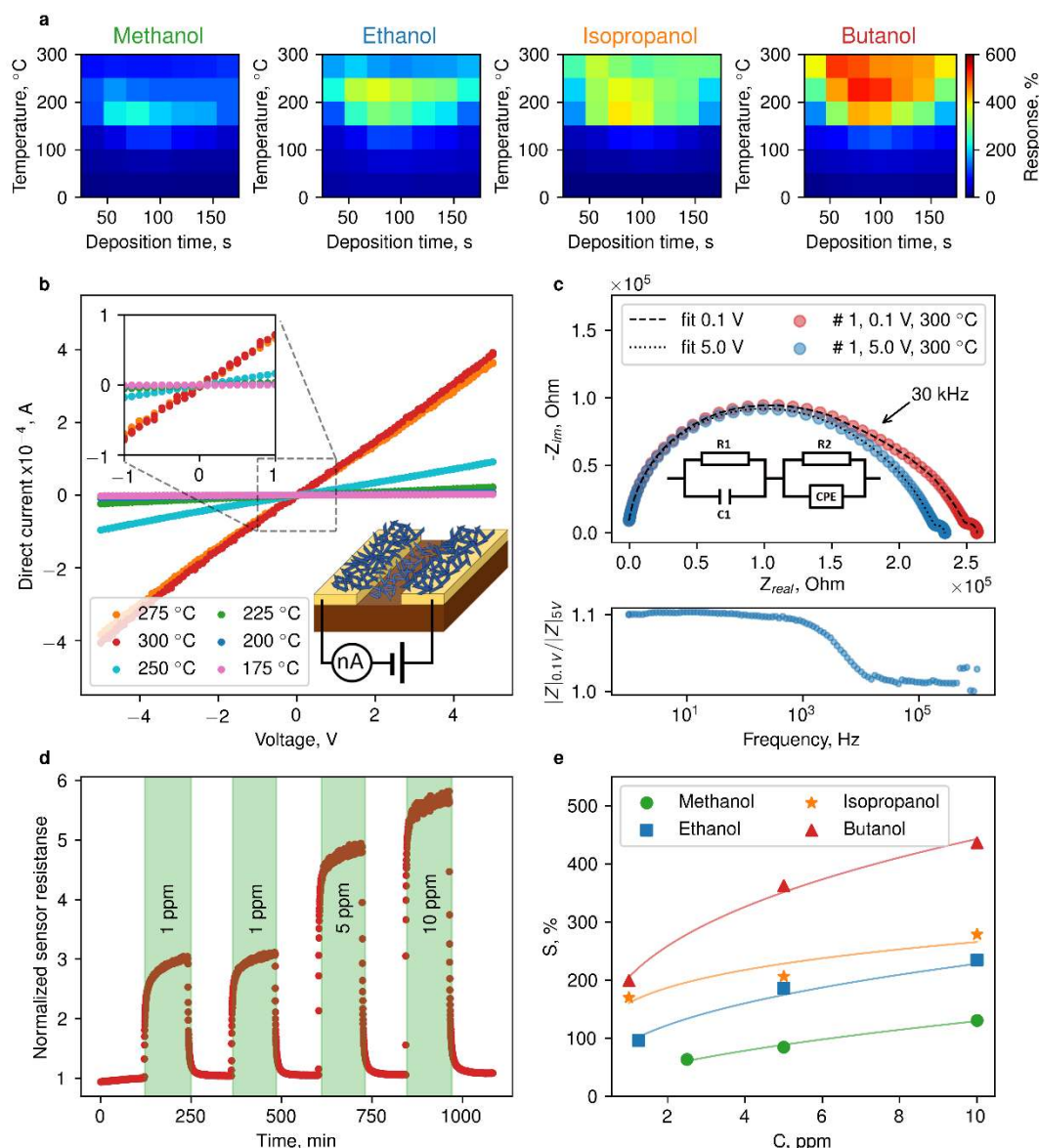

Figure 5. The characterization of gas-sensing properties of cobalt oxide quasi-2D nanoflake layer synthesized by electrochemical deposition over multielectrode chip: a) chemiresistive response to 10 ppm of analyte *versus* operating temperature for the sensors obtained under different deposition time; the average values of the response are shown for sensors deposited at [25:175] s range; b) I-V curve of the exemplary sensor under various operation temperatures, 175-300 ºC range, in pure air; insert: the cartoon scheme of the sensor; c) Nyquist plot and |Z|$_{0.1V}$/|Z|$_{5V}$ frequency dependence for the exemplary sensor at 300 °C in pure air; d) the resistance transient of the exemplary sensor under 275 °C operation when exposed to butanol vapors, 1-10 ppm concentrations, in the mixture with air; the resistance has been normalized by its value in air conditions; e) the dependence of chemiresistive response of exemplary sensor on the concentration of alcohol VOCs; methanol is colored by green, ethanol is blue, isopropanol is orange and butanol is red. The exemplary sensor is the one prepared at 75 s of deposition time, operation temperature 275 °C.
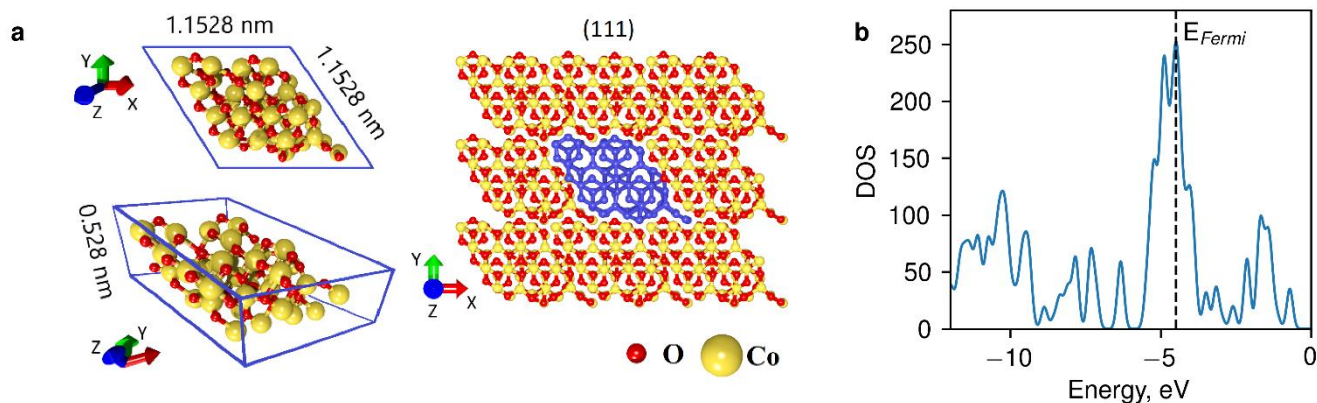
Figure 6. Atomic and electronic structure of Co_3O_4 thin layer, 0.528 nm, with (111) surface: (a) supercell geometric parameters and a layer fragment (the supercell is highlighted by blue colour); (b) the DOS plot.

Figure 1d that manages the receptor function of this material. Such a nano- transverse characteristic sizes of the oxide flakes seem to match or lower than the at-surface Debye length whose empirical estimation is still difficult in these hierarchical structures but should not exceed tens of nanometers.[84] The further advantage comes from the hierarchical origin of the grown layer which manages the transduction function of this sensor having percolating features as discussed above.

The chemiresistive performance of the sensors to alcohol VOCs is still maintained after 12-month shelf-storage (see ESI†, Figure S8). The more remarkable effect has a humidity whose appearance enhances the resistance, too, similar to alcohol ones (see ESI†, Figure S9). Therefore, in such a humid background, the sensor response to alcohols is reduced as we show, for instance in ESI† (Figure S8) with the example of sensor's exposure to butanol vapors at dry and humid, 30 rel. %, air. It indicates a competitive character of these vapors when interacting with cobalt oxide nanoflakes which requires further proper consideration.

Interaction of alcohol VOCs with Co_3O_4

To evaluate a chemiresistive response of the quasi-2D Co_3O_4 nanoflakes under consideration we have primarily simulated its receptor function, i.e. the interaction of alcohol molecules with the surface of this oxide layer. Particularly, we have tried out the influence of the molecules on the oxide electronic structure via calculating the Fermi level position which is shifted due to a charge transfer. For consideration, we constructed the unit cell of Co_3O_4 crystal with outer (111) surface containing 84 atoms as depicted in Figure 6a what also agrees well with our TEM observations. The unit cell has a rhombus shape with a side length of 1.1528 nm in the XY plane and 0.528 nm in the direction of the Z-axis. The electronic structure of the material was calculated using periodic boundary conditions in the XY plane. We applied translation vectors L1 (11.528, 0.0, 0.0), L2 (-5.764, 9.984, 0) and Monkhorst-Pack k-point grid, 5x5x1, for sampling the Brillouin zone and complete basis set of s-, p-, d-orbitals. The vector coordinates are given in angstroms.

The calculated density of states (DOS) is plotted in Figure 6b where Fermi energy is equal to -4.493 eV to be indicated by a dashed line. We observe the maximum DOS at the Fermi level that confirms a high efficiency of the (111) surface for sensor applications. Indeed, this indicates a rather good conductivity and high electron density that pre-determines the advanced chemical activity of the oxide. Since this surface plays a major role in the interaction of cobalt oxide crystal with alcohol molecules, we restricted the crystal thickness to be equal to 0.528 nm what corresponds to a single unit cell that was sufficient for modeling the interaction of alcohol molecules with crystal atoms at the surface. Employing single unit cells was enough to calculate the interaction of the cobalt oxide crystal with methanol, ethanol and isopropanol molecules while the butanol molecule was rather large at the XY plane and required an extended contact surface. Therefore, we considered the Co_3O_4 supercell which consisted of two unit cells with 168 atoms for all the alcohols.

The optimal energy position of alcohol molecule at the surface of Co_3O_4 crystal has been defined using a nonrelaxed 4D-potential energy surface (PES) scan without geometry optimization at each point for molecule/oxide crystal interaction in a process when molecule approaches the crystal. 4D PES reflects the dependence of molecule/crystal energy on four parameters, three rotation angles around X, Y, Z coordinate axes and molecule-crystal distance denoted as Z-axis. Such a nonrelaxed scan assumes a calculation of the energy of the molecule/crystal system without allowing the system to relax at each step of changing one of the four mentioned metric parameters. After the enumeration of all the metric parameters, we have built up a 4D PES whose analysis enabled us to identify the local energy minima and corresponding configurations of alcohol molecule with respect to the oxide crystal. For these configurations, we have performed an optimization of the atomic structure of alcohol molecules and crystal surface to reveal a configuration of the molecule-crystal system that is characterized by global energy minimum. Such a minimum indicates, on one hand, the depth of the potential well where the alcohol molecule gets in and, on the other hand, is equal to a potential barrier to overcome for the molecule to detach from the surface.
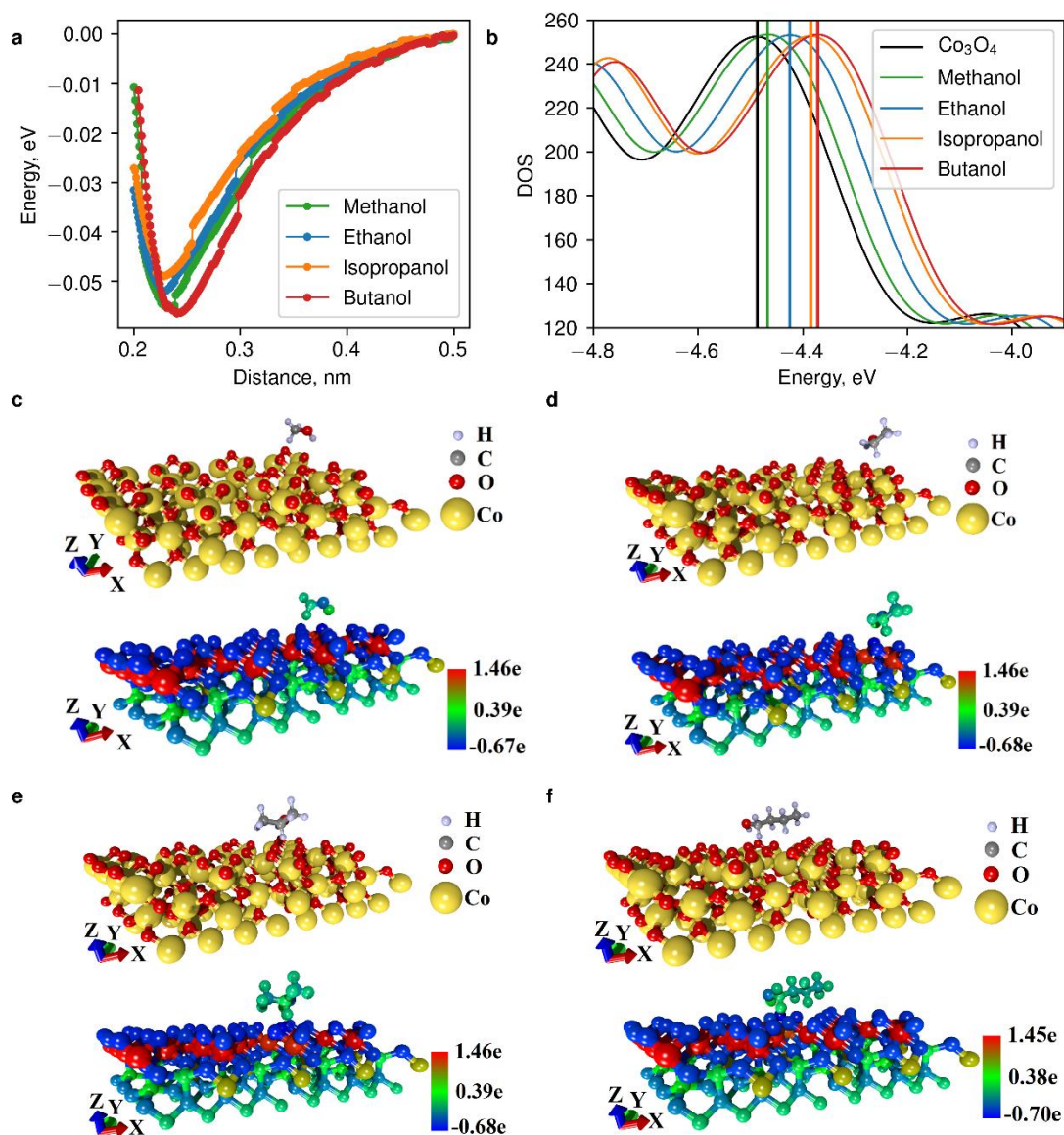
Figure 7. Modeling of interaction of cobalt oxide with alcohol molecules: a) interaction energy profile for the molecule approaching the oxide crystal surface, OX axis indicates the distance between the molecule and oxide surface; b) DOS plots for surface, free of adsorbed species, and the one with alcohol molecule; the vertical lines correspond to Fermi level; c), d), e) f) the animation of the appearance of supercell (111) surface of cobalt oxide with alcohol molecules and maps of electron charge density distribution in case of adsorption of methanol (c), ethanol (e), isopropanol (d), butanol (f).

The calculated energy profiles for molecule-crystal interaction in dependence on the distance from the molecule to crystal along Z-axis are presented in Figure 7a. The distance is varied from 0.1 nm to 1 nm with a step of 0.001 nm. The potential well depth increases with a rise of molecular weight. In general, the potential well depth ranges within 0.045- 0.054 eV what corresponds to 250–350 °C temperatures which, in turn, match well to ones optimal for yielding a chemiresistive effect in these Co_3O_4 nanoflakes. The observed abrupt transitions/drops in interaction energy are due to a drastic change in the orientation of alcohol molecules with respect to the crystal surface. When the energy approaches to 0 eV, the molecule and the crystal do not interact. Thus, we have an interaction of the alcohol molecules and the oxide starting at 0.5 nm distance as the molecule approaches the surface.

The chemisorption of alcohol molecules affects an electronic structure of cobalt oxide including a change in density of states, DOS. Figure 7b shows parts of DOS plots depicted close to the Fermi level; the Fermi level is also indicated for all the alcohol analyte cases of chemisorption. As the molecular weight of alcohol increases, the Fermi level shifts towards 0 eV. We have placed the calculated values of the Fermi level in Table 2. The peak of DOS intensity shifts accordingly, i.e. at the Fermi level we always observe a maximum DOS. Using calculated Fermi levels, we can estimate a resistance change as a chemiresistive effect induced in the oxide under chemisorption of alcohol molecules.

Table 2 The calculated characteristics of the interaction of alcohol molecules with cobalt oxide surface.

Alcohol molecules	Fermi level, eV	p/p_0, a.u.	Charge transfer, e (charge of an electron)	$\Delta R/R$, %
CH_3OH	-4.468	1.677	0.1532	18.3
C_2H_5OH	-4.422	4.219	0.1944	24.5
C_3H_7OH	-4.391	9.784	0.2333	33.2
C_4H_9OH	-4.374	11.169	0.3480	38.2

Indeed, in case of non-degenerate semiconductor the free charge carriers (holes) concentration in p-Co_3O_4 obeys the following equation:

$$p = p_0 \times \exp(\Delta E_F/kT) \qquad (5)$$

where p_0 is the hole concentration in the oxide prior its interaction with alcohol under background dry air, p is the hole concentration in the oxide after its interaction with alcohol molecule, k is Boltzmann constant, T is temperature, ΔE_F is a difference between Fermi level energies prior and following oxide surface's interaction with an alcohol molecule. This equation allows us to estimate the p/p_0 ratio as a relative change in conductivity when the carrier mobility is considered to be constant. The values of p/p_0 calculated for different alcohol molecules at T=573 K are tabulated in Table 2.

When the alcohol molecule interacts with the Co_3O_4 surface we observe a partial overlap of electron orbitals leading to a redistribution of electron charge density. Surface oxygen atoms draw the charge from hydrogen atoms of alcohol molecules. The optimum energy configurations of alcohol molecules set on the oxide surface are drawn in Figure 7 *on par* with the distribution of electron charge density at surface atoms and alcohol molecule atoms. In all the cases the charge is transferred from alcohol molecules to the oxide surface. As one can see from Table 2, the amount of the transferred charge directly follows enhancing the molecular weight of the alcohol in full accordance with experimental data.

The surface conductivity of these quasi-2D Co_3O_4 flakes was primarily approached in the absence of any chemisorbed species in two directions of current transfer, in [100] direction and [110] direction. We found that the resistance in [110] direction exceeds one in [100] direction by 2-3 times what suggests that current transfer should primarily follow the [100] direction. The calculation of $\Delta R/R_0$ in [100] direction has yielded the data (Table 2) which further supports the noted tendency that alcohol at higher molecular weight induces larger resistance changes. Still, we recognize that the described molecule adsorption should be followed by further chemical processes at the oxide surface and might include catalysis that would lead to the appearance of CO_2 and H_2O. However, these processes require further thorough theoretical consideration while even the primary interaction considered between alcohol molecules and the oxide indicates the experimentally observed trend.

Conclusions

In conclusion, we have synthesized quasi-2D nanoflakes of cobalt oxide by direct electrochemical process on the chip equipped with multiple electrodes to serve as a gas sensor. The employed method offers an almost ideal control over the deposited mass of the material at nanoscale morphology and enables its local growth that is advantageous for fine tuning material properties when developing gas sensors. The material is deposited as α-$Co(OH)_2$ and further is transformed to Co_3O_4 by annealing at the chip under temperature about 300 °C preserving quasi-2D morphology with a tendency to form pseudo-single crystal structures self-assembled as a matrix to bridge metal electrodes. Such a morphology favors exposure oxygen atoms/ions at (111) facets. The annealing results in the gradual decrease of surface water that was confirmed by MS and XPS measurements. The observed hierarchical layer consisting of the oxide nanoflakes is highly appropriate to get the efficient chemiresistive effect. The developed sensors show a high response to *low-ppm* alcohol VOCs at 250-300 °C operation temperature estimating to reach a *sub-ppm*-level of the detection limit. As revealed by impedance spectroscopy it stems not only from the nano-dimensionality of flake's walls but also from the inter-flake barrier contribution to be activated by temperature. Rather remarkable is that the chemiresistive response of Co_3O_4 nanoflakes exhibits a direct dependence on the alcohol molecular weight. We explain this behavior by DFT calculations due to enhanced charge transfer from larger molecules.

Conflicts of interest

There are no conflicts to declare.

Author contributions

F.S.F., M.U., A.G.N., and V.V.S. conceived the idea and designed the experiments. F.S.F., M.A.S., A.S.V., and M.S. fabricated the samples and sensor devices. F.S.F. and A.K.G. performed thermal analysis, XRD and SEM characterization. A.K.G. conducted FET measurements. F.S.F., M.U., A.M., and S.O. carried out the TEM, XPS characterization. M.A.I. carried out the *Z(f)* measurements. F.S.F., M.A.S., A.S.V., and V.V.S. conducted gas-sensing experiments. D.A.K. and O.E.G. performed DFT calculations. F.S.F., M.U., O.E.G., A.G.N., and V.V.S. discussed

and analysed the manuscript data. All authors contributed to writing the paper.

Acknowledgements

Notes and references

1 R. A. Potyrailo, *Chem. Rev.*, 2016, **116**, 11877–11923.

2 X. Liu, T. Ma, N. Pinna and J. Zhang, *Adv. Funct. Mater.*, 2017, **27**, 1702168.

3 G. Korotchenkov and V. V. Sysoev, in *Chemical sensors: comprehensive sensor technologies, Volume 4: Solid state devices*, ed. G. Korotchenkov, Momentum Press, LLC, New York, 1st edn., 2011, pp. 53–186.

4 Editorial: There's Plenty of Room at the Top. *Nat. Nanotechnol.*, 2019, **14**, 729.

5 Z. Meng, R. M. Stolz, L. Mendecki and K. A. Mirica, *Chem. Rev.*, 2019, **119**, 478–598.

6 T. Lin, X. Lv, Z. Hu, A. Xu and C. Feng, *Sensors*, 2019, **19**, 233.

7 J. Yang, Z. Zeng, J. Kang, S. Betzler, C. Czarnik, X. Zhang, C. Ophus, C. Yu, K. Bustillo, M. Pan, J. Qiu, L.-W. Wang and H. Zheng, *Nat. Mater.*, 2019, **18**, 970–976.

8 E. Llobet, E. Navarrete, F. E. Annanouch, M. Alvarado, E. González, J. L. Ramírez, A. Romero, X. Vilanova, M. Domínguez-Pumar, S. Vallejos and I. Grácia, in *2018 IEEE SENSORS*, 2018, pp. 1–4.

9 D. Zappa, V. Galstyan, N. Kaur, H. M. M. M. Arachchige, O. Sisman and E. Comini, *Anal. Chim. Acta*, 2018, **1039**, 1–23.

10 F. Meng, W. Qin, B. Li, H. Zhang, S. Wang, Y. Chang, M. Li and Z. Yuan, *IEEE Trans. Nanotechnol.*, 2019, **18**, 911–920.

11 J. M. Xu and J. P. Cheng, *J. Alloys Compd.*, 2016, **686**, 753–768.

12 H.-J. Kim and J.-H. Lee, *Sensors Actuators B Chem.*, 2014, **192**, 607–627.

13 J. Chen, X. Wu and A. Selloni, *Phys. Rev. B*, 2011, **83**, 245204.

14 D. Kohl, *Sensors and Actuators*, 1989, **18**, 71–113.

15 J. R. Stetter, *J. Colloid Interface Sci.*, 1978, **65**, 432–443.

16 W.-T. Koo, S. Yu, S.-J. Choi, J.-S. Jang, J. Y. Cheong and I.-D. Kim, *ACS Appl. Mater. Interfaces*, 2017, **9**, 8201–8210.

17 Y. Q. Liang, Z. D. Cui, S. L. Zhu, Z. Y. Li, X. J. Yang, Y. J. Chen and J. M. Ma, *Nanoscale*, 2013, **5**, 10916–10926.

18 S.-J. Hwang, K.-I. Choi, J.-W. Yoon, Y. C. Kang and J.-H. Lee, *Chem. – A Eur. J.*, 2015, **21**, 5872–5878.

19 Z. Yuan, J. Zhao, F. Meng, W. Qin, Y. Chen, M. Yang, M. Ibrahim and Y. Zhao, *J. Alloys Compd.*, 2019, **793**, 24–30.

20 C.-S. Lee, Z. Dai, S.-Y. Jeong, C.-H. Kwak, B.-Y. Kim, D. H. Kim, H. W. Jang, J.-S. Park and J.-H. Lee, *Chem. – A Eur. J.*, 2016, **22**, 7102–7107.

21 Q. Li, Y. Du, X. Li, G. Lu, W. Wang, Y. Geng, Z. Liang and X. Tian, *Sensors Actuators B Chem.*, 2016, **235**, 39–45.

22 K. Kamran, Z. Y. Shen, L. Da Wei, G. H. Rabiee, H. Xi, Z. Q. Ming, S. J. Feng, D. Stephen and L. Y. Feng, *Adv. Mater. Interfaces*, **4**, 1700294.

23 C.-Y. Liu, C.-F. Chen and J.-P. Leu, *Sensors Actuators B Chem.*, 2009, **137**, 700–703.

24 H. Nguyen and S. A. El-Safty, *J. Phys. Chem. C*, 2011, **115**, 8466–8474.

25 W. Y. Li, L. N. Xu and J. Chen, *Adv. Funct. Mater.*, 2005, **15**, 851–857.

26 Z. Dou, C. Cao, Y. Chen and W. Song, *Chem. Commun.*, 2014, **50**, 14889–14891.

27 A. P. Dral and J. E. ten Elshof, *Sensors Actuators B Chem.*, 2018, **272**, 369–392.

28 X. Lai, J. Li, B. A. Korgel, Z. Dong, Z. Li, F. Su, J. Du and D. Wang, *Angew. Chemie Int. Ed.*, 2011, **50**, 2738–2741.

29 Z. Li, Z. Lin, N. Wang, J. Wang, W. Liu, K. Sun, Y. Q. Fu and Z. Wang, *Sensors Actuators B Chem.*, 2016, **235**, 222–231.

30 Z. Zhang, L. Zhu, Z. Wen and Z. Ye, *Sensors Actuators B Chem.*, 2017, **238**, 1052–1059.

31 L. Li, C. Zhang, R. Zhang, X. Gao, S. He, M. Liu, X. Li and W. Chen, *Sensors Actuators B Chem.*, 2017, **244**, 664–672.

32 M.-Z. Yang, C.-L. Dai, P.-J. Shih and Y.-C. Chen, *Microelectron. Eng.*, 2011, **88**, 1742–1744.

33 A. Adán-Más, T. M. Silva, L. Guerlou-Demourgues, L. Bourgeois, C. Labrugere-Sarroste and M. F. Montemor, *J. Power Sources*, 2019, **419**, 12–26.

34 G. H. A. Therese and P. V Kamath, *Chem. Mater.*, 2000, **12**, 1195–1204.

35 Y. Lin, H. Ji, Z. Shen, Q. Jia and D. Wang, *J. Mater. Sci. Mater. Electron.*, 2016, **27**, 2086–2095.

36 F. S. Fedorov, J. Linnemann, K. Tschulik, L. Giebeler, M. Uhlemann and A. Gebert, *Electrochim. Acta*, 2013, **90**, 166–170.

37 R. S. Jayashree and P. V Kamath, *J. Mater. Chem.*, 1999, **9**, 961–963.

38 M. Dixit and P. Vishnu Kamath, *J. Power Sources*, 1995, **56**, 97–100.

39 J. van den Broek, S. Abegg, S. E. Pratsinis and A. T. Güntner, *Nat. Commun.*, 2019, **10**, 4220.

40 J. Goschnick, *Microelectron. Eng.*, 2001, **57–58**, 693–704.

41 V. V. Sysoev, I. Kiselev, M. Frietsch and J. Goschnick, *Sensors*, 2004, **4**, 37–46.

42 F. Fedorov, M. Vasilkov, A. Lashkov, A. Varezhnikov, D. Fuchs, C. Kübel, M. Bruns, M. Sommer and V. Sysoev, *Sci. Rep.*, 2017, **7**, 9732.

43 R. A. Washenfelder, C. M. Roehl, K. A. McKinney, R. R. Julian and P. O. Wennberg, *Rev. Sci. Instrum.*, 2003, **74**, 3151–3154.

44 V. V Sysoev, E. Strelcov, S. Kar and A. Kolmakov, *Thin Solid Films*, 2011, **520**, 898–903.

45 M. Elstner, D. Porezag, G. Jungnickel, J. Elsner, M. Haugk, T. Frauenheim, S. Suhai and G. Seifert, *Phys. Rev. B*, 1998, **58**, 7260–

7268.

46 M. Jiao, K. Li, W. Guan, Y. Wang, Z. Wu, A. Page and K. Morokuma, *Sci. Rep.*, 2015, **5**, 12091.

47 N. Khosravian, B. Kamaraj, E. C. Neyts and A. Bogaerts, *Sci. Rep.*, 2016, **6**, 19466.

48 "DFTB+," https://www.dftbplus.org/, accessed: January, 2020.

49 "About Kvazar / Nanokvazar," http://nanokvazar.ru/en/kvazar, accessed: January, 2020.

50 F. S. Fedorov, D. V. Podgainov, A. S. Varezhnikov, A. V. Lashkov, V. S. Dykin, M. E. Toimil-Molares and V. V. Sysoev, in *2015 IEEE SENSORS*, IEEE, 2015, pp. 1–4.

51 F. S. Fedorov, D. Podgainov, A. Varezhnikov, A. Lashkov, M. Gorshenkov, I. Burmistrov, M. Sommer and V. Sysoev, *Sensors (Switzerland)*, 2017, **17**, 1908.

52 S. Mishra, F. Lawrence, C. Mallika, N. K. Pandey, R. Srinivasan, U. K. Mudali and R. Natarajan, *Electrochim. Acta*, 2015, **160**, 219–226.

53 D. De, E. E. Kalu, P. P. Tarjan and J. D. Englehardt, *Chem. Eng. Technol.*, 2004, **27**, 56–64.

54 F. G. Cottrell, *Zeitschrift für Phys. Chemie*, 1903, 42U, 385.

55 A. J. Bard and L. R. Faulkner, *Electrochemical Methods: Fundamentals and Applications*, Wiley, New York, 2001.

56 O. A. Petrii and T. Y. Safonova, *J. Electroanal. Chem.*, 1992, **331**, 897–912.

57 C. Polatides and G. Kyriacou, *J. Appl. Electrochem.*, 2005, **35**, 421–427.

58 R. G. Ehl and A. J. Ihde, *J. Chem. Educ.*, 1954, **31**, 226.

59 A. S. Varezhnikov, F. S. Fedorov, I. N. Burmistrov, I. A. Plugin, M. Sommer, A. V. Lashkov, A. V. Gorokhovsky, A. G. Nasibulin, D. V. Kuznetsov, M. V. Gorshenkov and V. V. Sysoev, *Nanomaterials*, 2017, **7**, 455.

60 X. Liu, R. Yi, N. Zhang, R. Shi, X. Li and G. Qiu, *Chem. – An Asian J.*, 2008, **3**, 732–738.

61 P. Scardi, M. Leoni and R. Delhez, *J. Appl. Crystallogr.*, 2004, **37**, 381–390.

62 J. I. Langford and A. J. C. Wilson, *J. Appl. Crystallogr.*, 1978, **11**, 102–113.

63 A. Y. Polyakov, A. E. Goldt, T. A. Sorkina, I. V Perminova, D. A. Pankratov, E. A. Goodilin and Y. D. Tretyakov, *CrystEngComm*, 2012, **14**, 8097–8102.

64 M. J. Lai, C. C. Tasan and D. Raabe, *Acta Mater.*, 2016, **111**, 173–186.

65 N. Kattan, B. Hou, D. J. Fermín and D. Cherns, *Appl. Mater. Today*, 2015, **1**, 52–59.

66 M. C. Biesinger, B. P. Payne, A. P. Grosvenor, L. W. M. Lau, A. R. Gerson and R. S. C. Smart, *Appl. Surf. Sci.*, 2011, **257**, 2717–2730.

67 C. V Schenck, J. G. Dillard and J. W. Murray, *J. Colloid Interface Sci.*, 1983, **95**, 398–409.

68 B. J. Tan, K. J. Klabunde and P. M. A. Sherwood, *J. Am. Chem. Soc.*, 1991, **113**, 855–861.

69 J. L. Gautier, E. Rios, M. Gracia, J. F. Marco and J. R. Gancedo, *Thin Solid Films*, 1997, **311**, 51–57.

70 N. S. McIntyre and M. G. Cook, *Anal. Chem.*, 1975, **47**, 2208–2213.

71 L. Li, Y. Li, S. Gao and N. Koshizaki, *J. Mater. Chem.*, 2009, **19**, 8366–8371.

72 A. Rothschild and Y. Komem, *J. Appl. Phys.*, 2004, **95**, 6374.

73 A. Bobkov, A. Varezhnikov, I. Plugin, F. S. Fedorov, V. Trouillet, U.

Geckle, M. Sommer, V. Goffman, V. Moshnikov and V. Sysoev, *Sensors*, 2019, **19**, 4265.

74 C. M. Kleinlogel and L. J. Gauckler, *J. Electroceramics*, 2000, **5**, 231–243.

75 F. S. Fedorov, A. S. Varezhnikov, I. Kiselev, V. V. Kolesnichenko, I. N. Burmistrov, M. Sommer, D. Fuchs, C. Kübel, A. V. Gorokhovsky and V. V. Sysoev, *Anal. Chim. Acta*, 2015, **897**, 81–86.

76 U. Weimar and W. Göpel, *Sensors Actuators B. Chem.*, 1995, **26**, 13–18.

77 N. M. Beekmans and L. Heyne, *Electrochim. Acta*, 1976, **21**, 303–310.

78 T. van Dijk and A. J. Burggraaf, *Phys. status solidi*, 1981, **63**, 229–240.

79 J. E. Bauerle, *J. Phys. Chem. Solids*, 1969, **30**, 2657–2670.

80 R. Bouchet, P. Knauth and J.-M. Laugier, *J. Electroceramics*, 2006, **16**, 229–238.

81 J. Go, V. V Sysoev, A. Kolmakov, N. Pimparkar and M. A. Alam, in *2009 IEEE International Electron Devices Meeting (IEDM)*, 2009, pp. 1–4.

82 V. V Sysoev, J. Goschnick, T. Schneider, E. Strelcov and A. Kolmakov, *Nano Lett.*, 2007, **7**, 3182–3188.

83 V. V Kissine, V. V Sysoev and S. A. Voroshilov, *Appl. Phys. Lett.*, 2000, **76**, 2391–2393.

84 N. Barsan, C. Simion, T. Heine, S. Pokhrel and U. Weimar, *J. Electroceramics*, 2010, **25**, 11–19.